ORIGINAL PAPER

Gold-decorated Fe$_3$O$_4$ nanoparticles for efficient photocatalytic degradation of ampicillin: a chemometrics investigation

Naser Jalili-Jahani[1,2] · Bahram Hemmateenejad[1,2] · Mojtaba Shamsipur[3]

Abstract

Wastewater treatment for lowering down the amount of antibiotic drugs in environment is essential for preventing their harmful effects in the ecosystem and for diminishing the growing bacterial resistance. Here, gold-decorated Fe$_3$O$_4$ nanoparticles (NPs) were used for efficient photocatalytic degradation of ampicillin, investigated by UV/Vis absorbance spectrometry. The absorbance data matrices recorded in the course of reactions were analyzed using multivariate curve resolution-alternative least squares as a power chemometrics method. The resolved concentration profiles were composed of three intermediate species and one final product. The concentration profiles were fitted to a first-order kinetics and for the photodegradation experiments run (1) in the absence of photocatalyst, (2) in the presence of Fe$_3$O$_4$ NPs and (3) in the presence of Au-decorated Fe$_3$O$_4$ NPs, the rate constants of 0.023, 0.041 and 0.055 min^{-1} were obtained, respectively. We found that ampicillin undergoes fast photocatalytic degradation reaction, so that, in the presence of Fe$_3$O$_4$ NPs and Au-decorated magnetic NPs, it was completely converted to its photodegradation product in a few min (35 and 25 min, respectively). The results obtained by chemometrics analysis of the absorbance data agreed with those obtained by capillary electrophoresis.

Introduction

The significant growth of chemical drug production in this modern world causes emission of these chemical agents in the environment [1]. They come from different sources such as hospital's waste, pharmaceutical companies and even from human and animal exhausts [1]. Most of these drugs, which are found in surface water and groundwater, are harmful for ecosystem [2]. Among these, antibiotic drugs, which are consumed very much by human and animals, cause severe environmental risks, e.g., they are one of the main reasons for creating resistance bacteria [3–5]. So, wastewater treatment for lowering down the amount of these drugs in environment is essential for industries producing these products [6].

In the past, different methods have been suggested for the treatment of antibacterial drugs such as ampicillin (AMP). The first methods of choice were physisorption and chemisorption of the drug by absorbing materials [7, 8]. However, this procedure only transfers the drugs from one environment to another one, and hence, these methods do not diminish the environmental impact of the chemicals. The more efficient methods are forced degradations, e.g., acid or basic degradation, thermal degradation and oxidative degradation [9–12]. In recent years, attentions have been directed toward using photocatalyst for oxidative degradation of antibiotics [13]. Photocatalysts that are mainly metal oxide semiconductors (e.g., ZnO and TiO$_2$) produce reactive oxygen species (mainly hydroxyl radical) in aqueous solution upon irradiation with ultraviolet (UV) or daylight [13–15]. In the photocatalytic degradation process, the harmful species either is converted to other species of lower risk or ends with complete mineralization.

✉ Bahram Hemmateenejad
hemmatb@shirazu.ac.ir; hemmatb@sums.ac.ir

1 Chemistry Department, Shiraz University, Shiraz, Iran

2 Medicinal and Natural Products Chemistry Research Center, Shiraz University of Medical Sciences, Shiraz, Iran

3 Chemistry Department, Razi University, Kermanshah, Iran

Using nanoparticles as photocatalyst has attracted a lot of interest in these days [16–19]. They can provide higher catalytic efficiency and/or run the reaction in milder conditions. Among different reported nanocatalysts, magnetic nanoparticles based on Fe_3O_4 are interesting sources of photocatalysts since they can be easily collected by an external magnet for their recycling and regenerating [18, 19]. To obtain higher efficiencies, composites of Fe_3O_4 with noble metal nanoparticles have been used [20–22]. Previously, we showed that core–shell Fe_3O_4-Ag nanoparticles provided higher catalytic efficiencies compared to nanoparticles of Fe_3O_4 alone [23]. Ferrite nanoparticles decorated with Au nanoparticles are other types of Fe_3O_4 nanocomposites, which have shown enhanced catalyst properties [24, 25]. It should be noted that besides photocatalytic properties, Fe_3O_4 nanocomposites have been used as adsorbent for pollution removal from wastewater too [26 and references therein].

According to the environmental impact of AMP, degradation/mineralization of this antibiotic has been the subject of many studies [27–39]. Similar to other drugs, oxidation of AMP using metal oxide (e.g., WO_3/ZrO_2 [27] and ZnO/TiO_2 [28–31]) as photocatalyst has been studied by different research groups. Also, photo-oxidation of AMP by the Fenton reaction was reported [32]. Moreover, BiOCl [33] and its combination with Bi_2O_3 [34], both supported on graphene sane and chitosan, were used for photocatalytic mineralization of AMP. In addition to conventional photocatalysts, nanocomposites (ZnO/$ZnWO_4$ nanocomposite [35], trimetallic nanocomposite of La/Cu/Zr [36] and ZnO/polyaniline nanocomposite [37]) have been used for remediation of AMP. Last but not least, a composite of Fe_3O_4 magnetic nanoparticles with TiO_2 and Ag nanoparticles (Fe_3O_4@TiO_2@Ag) was synthesized by Zhao et al. [38] and used for photocatalytic degradation of AMP.

A mathematical and statistical modeling of the photocatalytic process is always subjected to great interests for understanding both fundamental phenomena and steering reaction pathway toward desire product(s) [39–41]. UV/Vis absorption spectroscopy has been considered as an analytical method owing to its low cost, speed and simplicity of measurements. However, because of band overlapping, it has limited applications in multicomponent systems. However, since the development of chemometrics methods, the chemists have been able to monitor and study reaction kinetics and equilibrium using UV/Vis absorbance spectroscopy [42, 43]. Multivariate curve resolutions (MCRs) are groups of chemometrics methods that can resolve the absorbance data matrix, recorded in a course of a chemical reaction, to the pure contribution of the species involved in the reaction [44, 45]. Multivariate curve resolution-alternative least square (MCR-ALS) technique is one of the efficient MCR methods that have been found major popularity in the chemometrics literature [46, 47].

In this paper, the photodegradation of AMP in the presence of gold-decorated Fe_3O_4 nanoparticles as photocatalyst is investigated using UV/Vis absorbance spectroscopy. The absorbance data recorded in the course of photodegradation reactions are analyzed by the MCR-ALS method to get insight into the mechanism of the reaction. By comparing the photodegradation in the presence and absence of photocatalyst, a plausible reaction mechanism is suggested.

Experimental

Chemicals

Analytical-grade reagents were used. Hydrogen tetrachloroaurate (III) trihydrate ($HAuCl_4.3H_2O$, 99.9%), sodium citrate ($Na_3C_6H_5O_7$), $FeCl_2 \cdot 4H_2O$ (> 98.0%), $FeCl_3 \cdot 6H_2O$ (> 99.0%), $NH_3 \cdot H_2O$ (25.0–28.0%) and HPLC-grade solvents (purity 99.0%) such as methanol and ethanol were purchased from Sigma-Aldrich. Pure powder of ampicillin trihydrate ($\geq$ 99.0%) was purchased from Farabi Pharmaceutical Company, Iran. Sodium dodecyl sulfate (SDS) was purchased from Merck, Germany.

Solutions of Britton–Robinson buffers were prepared in 0.04 M concentration. AMP stock solutions (C_1:150.0, C_2:250.0 and C_3:350.0 μM) were prepared daily by dissolving its required amounts in 5.0% ethanolic buffer solution (50.0 mL) of pH 7.0. High-purity water purified with the Milli-Q system was used in all experiments.

Instruments

A diode-array Hewlett Packard (HP) 8452A spectrophotometer (Avondale, PA, USA) was used for absorbance measurements. An Agilent capillary electrophoresis (CE) system (Waldbronn, Germany) equipped with a 56.0-cm fused silica capillary of 50.0 μm internal diameter was used. Conditioning of capillary was done by flushing with 0.1 mol/L NaOH for 20.0 min followed by water for 10.0 min. Determination was performed at 30.0 kV and 25.0 °C (under applied pressure of 15.0 mbar) in 10.0 min; under these conditions, the current was 49.0–50.0 μA. UV detection was at 215.0 nm. Peak area was used for the quantification.

A Hitachi S-4300 (Japan) instrument was employed to record the transmission electron microscopy (TEM) images. A PHILIPS PW-1840 diffractometer was used to record the X-ray diffraction (XRD) spectra. The Fourier transform infrared (FTIR) spectra were recorded using a Shimadzu Fourier transform infrared 8300 spectrophotometer. Hysteresis loop measurements (for determination of magnetization) were taken with a Quantum Design PPMS Model 6000 magnetometer at 25.0 °C. The pH of solutions was measured by a Metrohm 744 pH meter (Switzerland).

An external magnet bar of 5.0 cm × 5.0 cm × 3.0 cm and power of 1.46 T were used for the accumulation of magnetic nanoparticles (NPs).

Procedure

Synthesis of Au-decorated Fe_3O_4 nanoparticles

The Au-decorated F_3O_4 nanoparticles were synthesized following the method suggested by Lee and coworkers [48, 49], which was the modified version of the synthetic method reported by Grabar et al. [50]. A 1.622 g portion of $FeCl_3 \cdot 6H_2O$ and a 0.9941 g portion of $FeCl_2 \cdot 4H_2O$ were dissolved in 40.0 mL already deaerated deionized water under a constant mechanical stirring and N_2 purging. A 5.0-mL aliquot of ammonia solution of 28.0% (w/v) was added, after complete dissolving the reagents. The resulting solution was stirred for 10.0 min, and then, sodium citrate (4.4 g) was added. Stirring was continued for 30 min, while the temperature increased to 90.0 °C. Cooling the reaction mixture resulted in the formation of the black precipitate of F_3O_4. After rinsing the precipitate thoroughly with distilled water, a magnet was used to separate the precipitate from the supernatant.

Next, a 20.0 mL portion of 0.5 mM $HAuCl_4$ solution was transferred in a backer and was heated and stirred vigorously until boiling. A rapid addition of 4.0 mL of the Fe_3O_4 NPs solution prepared from the previous step (approximately 0.136 μM) resulted in a continuous color change from brown to burgundy. After 10.0-min stirring, the heating power turned off while stirring continued till the solution's temperature cooled to room temperature. The $AuCl_4^-$ species can be reduced by the sodium citrate, which capped on the surface of Fe_3O_4 NPs. This causes the formation of Au islands on the magnetic core. Magnetic centrifugation of the resultant solution at 6500 rpm precipitated the Au-decorated Fe_3O_4 NPs. Centrifugation was repeated three times, each continued for 30 min. The precipitates were rinsed with deionized and re-dispersed. The final solution appeared dark purple.

Photocatalytic degradation of AMP

The direct and photocatalytic degradation of AMP was carried out in a homemade photodegradation setup reported by us previously [23]. Prior to illumination, a suspension of 50.0 mL (equal volumes) from AMP and photocatalyst (Au-decorated Fe_3O_4 NPs) solutions with different concentrations was stirred in the dark. Then, photocatalytic degradation was started by turning on the light sources (two 254-nm UV lamps; 450 mm, 15 W; Philips, Netherlands). Sampling from the reaction solution (3.0 mL) was done at fixed time intervals. The samples were exposed to an external magnetic field for separation of magnetic NPs from the reaction mixture and then were analyzed by recording the UV–Vis absorbance spectra in the wavelength interval of 200.0 and 500.0 nm.

For each photocatalytic degradation run, the recorded absorbance spectra were digitized in 1.0-nm intervals and those collected throughout the experiment were provided in a data matrix **D**. The rows of the data matrix are the UV–Vis absorbance spectra at the sequential time intervals, and the columns represent absorbance–time profiles at different wavelengths. Since in the wavelength interval of 350 and 500 nm no significant absorbance data were observed, the absorbance readings in the range of 200–350 nm (150 absorbance readings per spectrum, which are the number of columns of **D**) were selected for future analyses. The sampling time intervals were varied from experiments to experiments. Thus, the data matrices of different runs did not have the same number of rows.

Results and discussion

Characterization of the gold-decorated magnetic nanoparticles

Figure 1 displays representative TEM images of bare and Au-decorated Fe_3O_4 NPs. They clearly show that Fe_3O_4 NPs, whose solution is yellow in color, have almost spherical shape with average size of about 10.0 nm. Additionally,

Fig. 1 TEMs of the as-prepared spherical-shaped bare (left) and Au-decorated (right) magnetic NPs
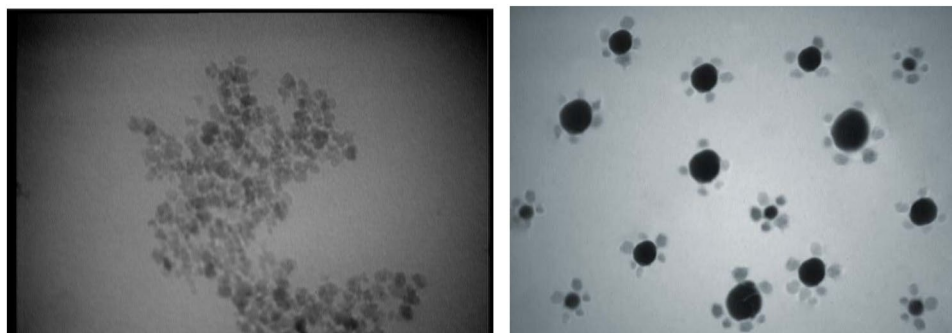
the Au-decorated Fe_3O_4 NPs, whose solution is purple in color, have also spherical shape but are larger in size (about 20.0 nm).

Figure 2A shows the FTIR spectra of citrate-capped Fe_3O_4 NPs (a) and Au-decorated Fe_3O_4 NPs (b). The shift in frequency of C=O vibration from 1578.0 cm^{-1} (for citric acid) to about 1560.0 cm^{-1} (for Fe_3O_4 NPs) confirms the binding of a citrate to the surface of Fe_3O_4 NPs [51]. Furthermore, the observed peak at around 575.0 cm^{-1} can be attributed to the Fe–O stretching mode of the citrate-capped Fe_3O_4 NPs [52].

The XRD pattern of Fe_3O_4 NPs (Fig. 2B) had diffraction peaks at 30.05°, 35.33°, 43.01°, 53.39°, 56.87° and 62.48° which can be, respectively, indexed to the (220), (311), (400), (511) and (440) planes of Fe_3O_4 in a cubic phase [53]. These diffraction peaks agree also with those previously reported by Mandal et al. [54].

The UV–Vis absorbance spectra are shown in Fig. 2C. The bare Fe_3O_4 NPs solution does not show significant absorbance peak in the visible region (curve a), whereas the solutions of Au-decorated Fe_3O_4 NPs represent surface plasmon peaks in the wavelength ranges of 540–600 nm (curves $b_1 \rightarrow b_6$), indicating the formation of Au islands [49, 55]. The observed blueshift from 600.0 to 530.0 nm (from b_1 to b_6) because of increase in the reactive volume of Au precursors agrees with those observed previously by Lee et al. [48, 49]. As stated by Zhou et al. [49], the observed peak broadness may be caused by non-uniform Au islands around the Fe_3O_4 cores.

The hysteresis loops of Fe_3O_4 and Au-decorated Fe_3O_4 NPs are shown in Fig. 2D. The Ms of Fe_3O_4 NPs was 66.8 $emug^{-1}$, whereas it dropped significantly for Au-decorated Fe_3O_4 NPs (Ms of 16.2 $emug^{-1}$), but these nanoparticles still can be considered nearly paramagnetic [56]. As shown in the inset of Fig. 2D, the Au-decorated Fe_3O_4 NPs were separated using a magnet. The nanoparticles were attached to the interior wall of the sample container, and the rest of sample solution turned very clear and transparent. Interestingly,
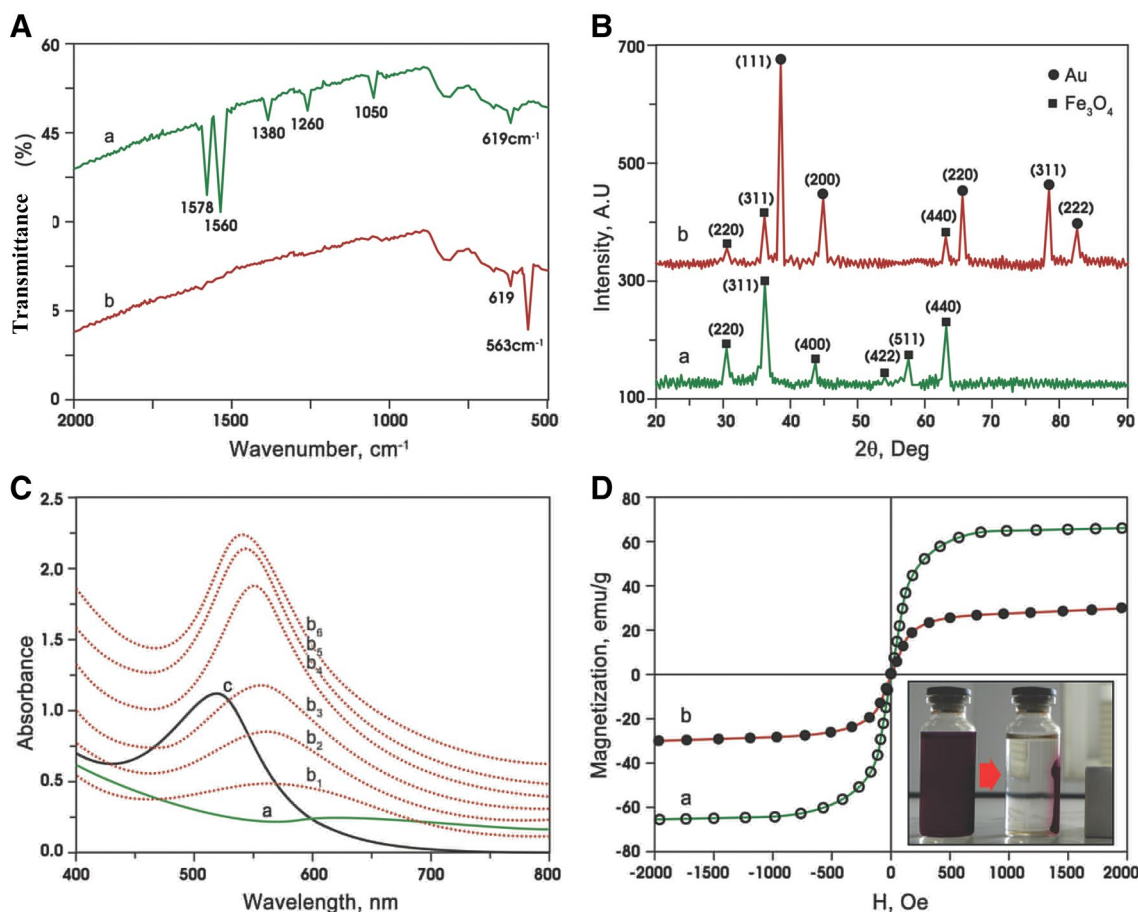

Fig. 2 A FTIR spectra of (a) Fe_3O_4 and (b) Au-decorated Fe_3O_4 NPs. B XRD pattern of (a) Fe_3O_4 and (b) Au-decorated Fe_3O_4 NPs. C UV–Vis absorption spectra of (a) Fe_3O_4, ($b_1 \rightarrow b_6$) Au-decorated Fe_3O_4 with the increase in reactive volume of Au precursors solution from b_1 to b_6 and (c) Au NPs. D Hysteresis loops recorded at room temperature of (a) Fe_3O_4 and (b) Au-decorated Fe_3O_4 NPs. Inset shows photograph of the Au-decorated Fe_3O_4 NPs suspension after magnetic separation by an external magnet

after removing the magnet, the nanoparticles were re-dispersed in aqueous solutions.

Photocatalytic degradation of AMP

The photocatalytic degradation of AMP was monitored by the spectrophotometric method, processed by multivariate curve resolution-alternative least squares (MCR-ALS) as one of the powerful and advanced data analysis methods. To do so, as explained in "Photocatalytic degradation of AMP" section, for each degradation experiment, a data matrix of digitized absorbencies, recorded at different irradiation times, was provided. In total, nine photodegradation experiments were run; three solutions of AMP with initial concentrations of 150.0, 250.0 and 350.0 μM were investigated in three different conditions (in the absence of photocatalyst, in the presence of Fe_3O_4 NPs and in the presence of Au-decorated Fe_3O_4 NPs). It should be noted that all experiments were conducted at pH 7.0.

As an example, the changes in the absorbance spectra of AMP over irradiation time, in the absence and presence of Au-decorated Fe_3O_4 nanocatalyst for one concentration of AMP, are depicted in Fig. 3 and Fig. S1 of supplementary material. Irradiation of AMP solutions with 254-nm UV light caused an increase in absorbance peak of around 210 nm (with slight redshift) in accompanying with the appearance of new absorbance speak at around 300 nm. A faster change in absorbance data is observed when the AMP is irradiated in the presence of nanocatalyst.

MCR-ALS analysis decomposes a bilinear data matrix (**D**) of, for example, absorbance data, recorded during an evolutionary process for a multicomponent system, into two new matrices of **C** and **S** according to the Beer–Lambert law of absorbance additivity of mixtures:

$$\mathbf{D} = \mathbf{C}\,\mathbf{S}^{T} + \mathbf{E} \tag{1}$$

where **E** stands for non-modeled part of **D** or noise and the superscript "T" denotes matrix transpose. Each corresponding column of **C** and **S** explains the concentration profile (concentration change as a function of time) and pure spectra (molar absorptivity at different wavelengths) of a given species in the system, respectively. MCR-ALS starts with an initial estimate for either **C** or **S** and then continues by iterative calculating of the complementary matrix till convergence, at which there is no improvement in the lack of fit error.

To avoid incorrect estimation of the number of chemical factors because of possible rank deficiency and to get more accurate results with lower degree of rotational ambiguity, MCR-ALS analysis was run in multiset analysis manner. In this context, an extended data matrix was obtained by column-wise augmentation of the data matrices, which is obtained in nine different conditions:
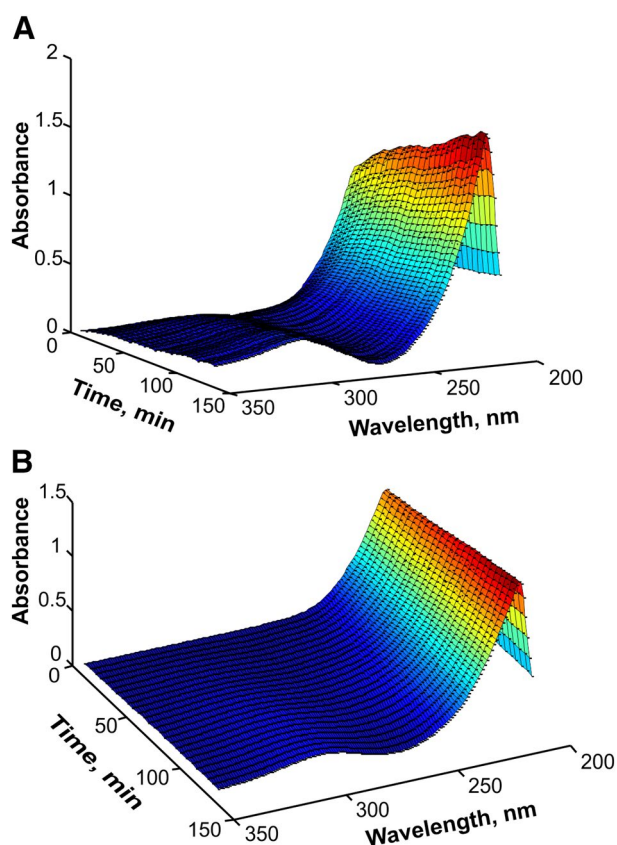

Fig. 3 Changes in the absorbance spectra of AMP aqueous solution (250.0 μM) at different irradiation times: **A** in the presence of Au-decorated Fe_3O_4 NPs and **B** in the absence of photocatalyst

$$\mathbf{D}_{aug} = \left[\mathbf{D}_1; \mathbf{D}_2; \mathbf{D}3; \ldots; \mathbf{D}_9\right] \tag{2}$$

In the column-wise augmentation, the original $\mathbf{D}i$ matrices share the same columns (here wavelengths). Bilinear decomposition of the extended data matrix by MCR-ALS results in different concentration profiles sharing the same pure spectra:

$$\mathbf{D}_{aug} = \left[\mathbf{C}_1; \mathbf{C}_2; \mathbf{C}3; \ldots; \mathbf{C}_9\right]\mathbf{S}^{T} \tag{3}$$

MCR analysis starts with finding the number of chemical species (or chemical rank) in the system. Rank analysis showed five components in the system (Fig. S2 of Supplementary section). As shown in this figure, after inclusion of five factors, no significant changes in eigenvalues are observed. Besides, the red line depicted in the figure indicates that the eigenvalue number 6 is located in around the instrumental noise level. This result was also confirmed by EFA. As shown in Fig. S2, a large separation is observed between the first five eigenvalues and the rest of ones. Additionally, the loading plots (Fig. S3) demonstrate that the first five PCs contained systematic variances and the

sixth one represents noise variances. Furthermore, MCR-ALS analysis was run with different number of factors and the residuals were plotted. For number of factors < 5, the residuals represent systematic variations. However, for number of factor of 5, we do not observe a significant systematic variation in residual. The more increase in the number of factors did not effect on the structure of residuals. All these rank analysis methods suggest that five chemical components are most probable.

In the self-modeling curve resolution methods like MCR-ALS, the implementation of natural constraints helps the model to converge to more chemically meaningful solutions. Here, both concentration profiles and pure spectra were subjected to nonnegativity constraint, whereas unimodality constraint was applied on the concentration profiles. When no local rank information is available, implementation of selectivity constraint would be very helpful. In our case, the spectra of AMP solutions kept in the dark were used to implement selectivity. Finally, since the studied systems were closed, all photodegradation products come from initial AMP, and

we implemented closure constraints to the concentration profiles.

The resolved concentration profiles and pure spectra of AMP after convergence of the constrained MCR-ALS model are given in Fig. 4. The concentration profiles are composed of one starting species, three intermediate species and one final product. Analysis of the kinetics behavior of AMP (as reactant) suggests that the direct and catalytic photodegradation kinetics of AMP can be divided into two regions. In the kinetics region before half-life, the concentration profile of AMP fits to a zero-order kinetic law. In the second kinetics region, which is after half-life, the concentration profiles are best described by a first-order kinetics.

We found that AMP undergoes fast photocatalytic degradation reaction, so that, in the presence of Au-decorated magnetic NPs, it is completely converted to its photodegradation product in a few min. The kinetics of photochemical reactions should obey zero order according to the Einstein photochemical law. However, the inhibitory effect of the reaction product(s) on the photodegradation kinetics alters the reaction kinetic from zero order to the first order.
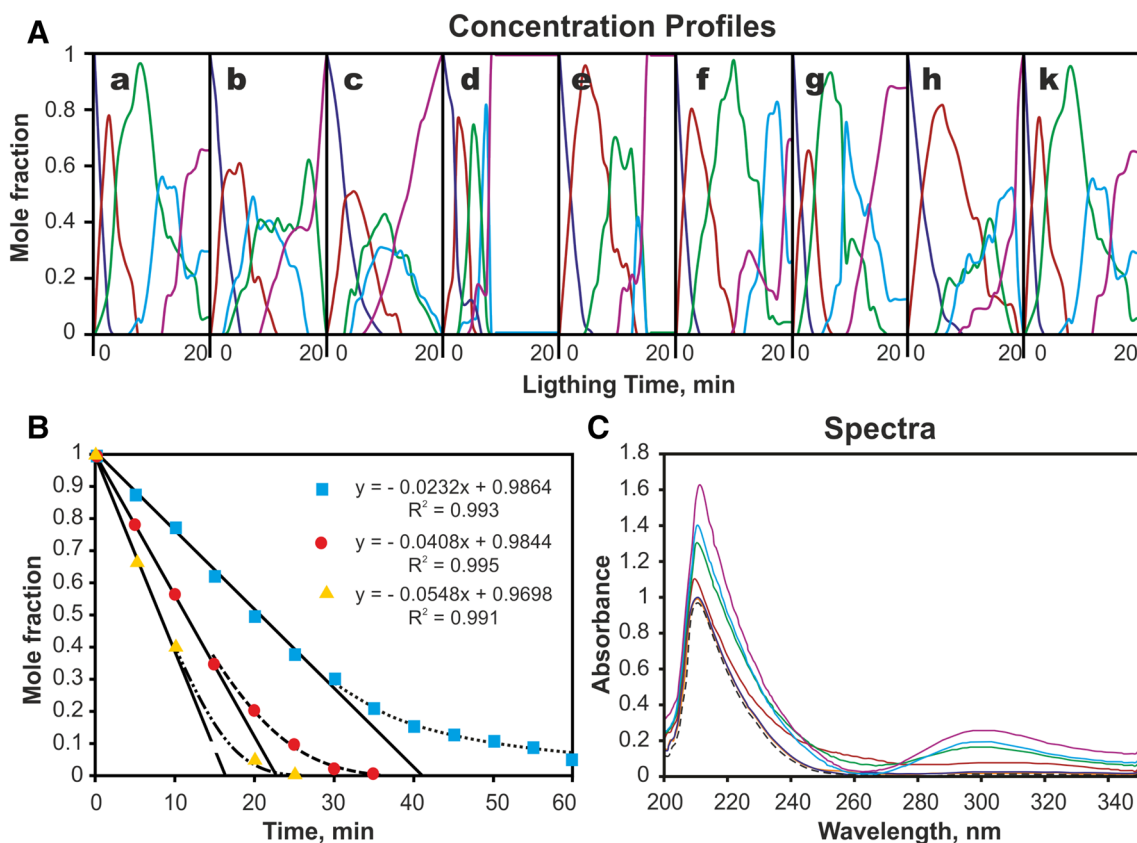

Fig. 4 Results of MCR_ALS: **A** resolved concentration profiles at nine different photodegradation runs: in the absence of photocatalyst (a, b and c), in the presence of Fe_3O_4 NPs (d, e and f) and in the presence of Au-decorated Fe_3O_4 NPs (g, h, k). The concentrations of AMP were 150.0 μM (a, d and G), 250.0 μM (b, e and h) and 350.0 μM (c, f and k). **B** Fitting the initial part of the AMP concentration profile to zero-order kinetics in the absence of photocatalyst (■), in the presence of Fe_3O_4 NPs (●) and in the presence of Au-decorated Fe_3O_4 NPs (▲) and **C** resolved pure concentration profiles

Previous studies on the photocatalytic degradation of AMP have also suggested a first-order kinetic mechanism [29, 30, 36, 57]. To have a quick snapshot on the rate of the photocatalytic degradation of AMP, the initial part of the concentration profiles of AMP (Fig. 4B) at different conditions was fitted to the first-order rate law and the respective rate constants were calculated. As shown in the inset of Fig. 4B, the rate constants, which are the slope of the concentration–time curves, are 0.023, 0.041 and 0.055 min^{-1}, in the absence of photocatalyst, in the presence of Fe_3O_4 NPs and in the presence of Au-decorated Fe_3O_4 NPs, respectively. So, higher kinetics rate in the presence of Au-decorated Fe_3O_4 NPs is obvious. The concentration–time decay of AMP shown in Fig. 4B implies that in the absence of nanocatalyst, AMP does not degrade totally such that after 60-min irradiation, 90% of AMP remains intact. However, in the presence of Fe_3O_4 NPs, complete photodegradation is achieved in 35 min of UV irradiation. On the other hand, Au-decorated Fe_3O_4 NPs increases the rate of photodegradation and shortens the photodegradation time to 25 min.

Comparing the slope of the kinetic curves and the required times for complete photodegradation of AMP reveals a 30% higher efficiency for Au-decorated Fe_3O_4 NPs relative to Fe_3O_4 NPs. It is worthy to mention that the number of degradation products and the kinetic curves of the species produced during the photodegradation study of AMP (Fig. 4A) are similar for non-catalytic and catalytic degradation of AMP. This suggests that the used nanocatalysts in this study did not change the photodegradation pathway and just changed the rate of degradation. The calculated pure spectrum of AMP (Fig. 4C) agrees very well the experimental spectrum, indicating the high accuracy of the MCR results.

For confirmation of the kinetic pathway suggested by MCR-ALS, photocatalytic degradation of AMP was also monitored by capillary electrophoresis. AMP stock solution and photocatalytic degraded samples were injected to CE, separately. As shown in Fig. 5, the presence of four photodegradation products is evident. The electropherogram of one product, which is the main photodegradation product, is appeared close to that of AMP, suggesting that this species is very similar to AMP. The peaks of other three products are appeared far from AMP but close to each other, explaining that these species have different chemical structures from AMP.

Photocatalytic mechanism of the Au-decorated magnetic nanoparticles

Previously, a charge separation mechanism for photocatalytic activity of Ag-Fe_3O_4 nanocomposite has been suggested [23]. It seems that a similar mechanism would be applied for Au-decorated Fe_3O_4 NPs. To probe the charge
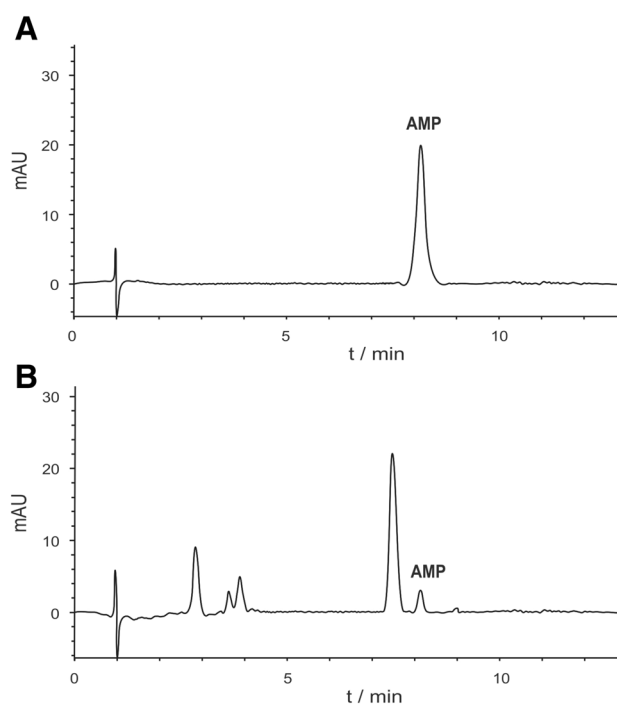

Fig. 5 Recorded electropherograms from AMP stock solution (**A**) and a photocatalytic degraded sample (**B**)

transfer between Fe_3O_4 core and Au islands, we first prepared colloidal Au-decorated Fe_3O_4 NPs (0.046 M) in ethanol toluene with constant stirring (steady-state photolysis experiments). The average particle diameter is in the range of 20.0–25.0 nm. The suspension was purged with N_2 gas and was then subjected to UV illumination for 2.0 h. The UV-irradiated sample cell was then transferred to the spectrophotometer to record the absorption spectra. A blueshift in the surface plasmon absorption peak of Au islands, similar to those found for Ag-Fe_3O_4 nanocomposite, was observed. A redshift and the slight bleach of surface plasmon absorption peak of Au islands in the presence of redox couples in solution were also observed. This is likely to be caused by the dampening of the Au plasmon band as holes are accumulated around the Au islands on the magnetic core as well as solution–catalyst interfacial electron transfer. According to these observations, which are consistent with our previous finding [23] and in accordance with the suggested photocatalyst mechanism for Fe_3O_4-based nanocomposites [58, 59], the formation of OH free radical is suggested as the plausible mechanism for photocatalytic property of the Au-decorated Fe_3O_4 NPs. Similar mechanism (hydroxy radical production) was observed for Au@TiO2 nanoparticles by Khan et al. [60].

According to the report of Hou and Poole [61], the degradation product of AMP, whose peak is close to that of AMP (Fig. 5), can be attributed to the compound produced
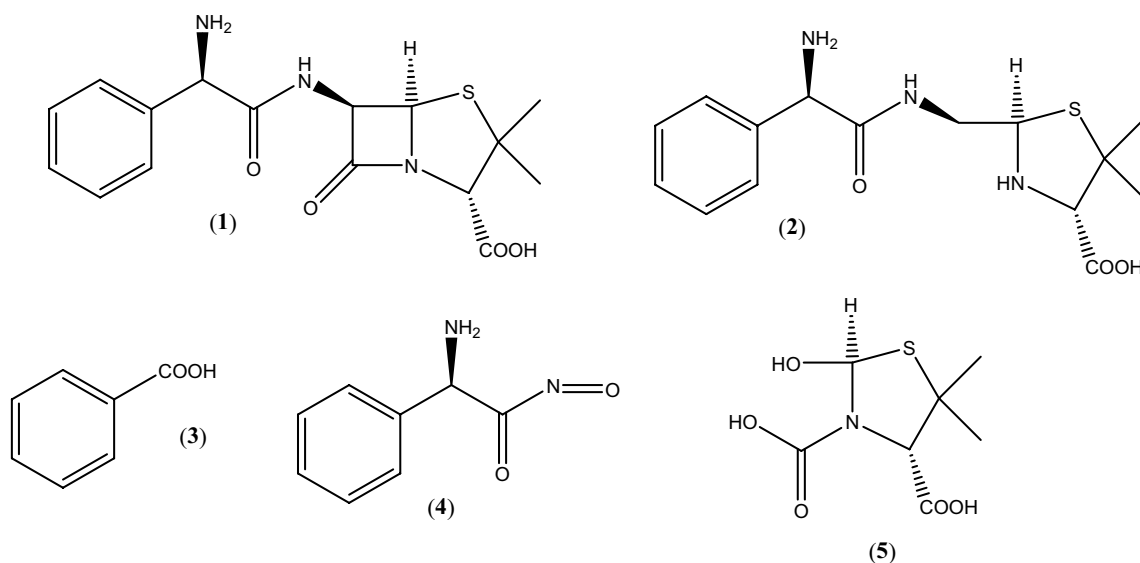
Fig. 6 Chemical structures of AMP (1) and its plausible degradation products (2–5)

Table 1 Comparing the photodegradation efficiency of the Au-decorated magnetic NPs with some of the previously reported photocatalysts for degradation of AMP

Catalyst	Degradation efficiency		First-order rate constant	References
	Time (min)	Yield (%)		
WO$_3$–ZrO$_2$–Ru	180 min	97	NR	[27]
TiO$_2$	30 min (with H$_2$O$_2$)	100	0.003 min^{-1}	[29]
ZnO	180 min	100	0.015	[30]
Activated carbon-supported ZnO/ZnWO$_4$ nanocomposite	60 min	93	NR	[35]
La/Cu/Zr trimetallic nanoparticles	240 h	86	0.006	[36]
ZnO/polyaniline nanocomposite	120 min	41	NR	[37]
60%WO$_3$/BiOCl stacked to graphene sand composite	60 min	~100	0.004	[62]
Gold-decorated Fe$_3$O$_4$ nanoparticles	25 min	100	0.055	This work

NR not reported

from beta-lactam ring cleavage (compound **2** in Fig. 6). In addition, the peaks appear at early times of the electropherogram which can be attributed to smaller molecules of higher polarity (or bearing more charges). As suggested by Olad and Nosrati [62], these small molecules can be produced by cleaving of the acetamide bonds (compound **3**, **4** or **5** in Fig. 6).

Conclusions

Direct and catalytic photodegradation studies were done on AMP in the absence and presence of Au-decorated magnetic NPs, respectively. These studies used three and two different initial concentrations for AMP and photocatalysts,

respectively. For each initial concentration of AMP, three experimental runs in the absence and presence of photocatalysts have been mapped. The recorded column-wise augmented matrix $\mathbf{D_{aug}}$ was subjected to MCR-ALS analysis. It should be noted that all experiments were conducted at pH value equal to 7.0. MCR results revealed that the extracted concentration profiles and pure spectra in the nine recorded data sets are analogous and show that the AMP in the absence or presence of photocatalysts follows approximately similar photodegradation pathways.

The extracted concentration profiles of AMP describe that it undergoes fast photocatalytic degradation in the presence of the photocatalysts such that in the presence of Au-decorated magnetic NPs, it is completely converted to its photodegradation product in a few min. Both chemometrics

analysis and capillary electrophoresis revealed the formation of five photodegradation products for AMP. By comparing the concentration profiles of the photodegradation products in the presence and absence of photocatalyst, we found that the photocatalysts do not change the reaction pathway but increase the reaction rate.

In comparison with the previously reported photocatalysts for degradation of AMP (Table 1), the Au-decorated magnetic NPs resulted in much higher efficiency. It behaves similar to TiO$_2$, but it does not need H$_2$O$_2$, which is a very harmful chemical. In addition, the largest rate constant has been obtained in our study.

References

1. D.G.J. Larsson, C. de Pedro, N. Paxeus, J. Hazard. Mater. **148**, 751–755 (2007)
2. E.J. Rosi-Marshall, D. Snow, S.L. Bartelt-Hunt, A. Paspalof, J.L. Tank, J. Hazard. Mater. **282**, 18–25 (2015)
3. K. Kümmerer, Chemosphere **75**, 417–434 (2009)
4. N. Kemper, Ecol. Indic. **8**, 1–13 (2008)
5. M. González-Pleiter, S. Gonzalo, I. Rodea-Palomares, F. Leganés, R. Rosal, K. Boltes, E. Marco, F. Fernández-Piñas, Water Res. **47**, 2050–2064 (2013)
6. E. Bloomer, M. McKee, J. Public Health Policy **39**, 389–406 (2018)
7. M. Grassi, G. Kaykioglu, V. Belgiorno, G. Lofrano, Removal of emerging contaminants from water and wastewater by adsorption process, in *Emerging Compounds Removal from Wastewater*, Springer Briefs in Molecular Science, ed. by G. Lofrano (Springer, Dordrecht, 2012)
8. G. Crini, E. Lichtfouse, L.D. Wilson, N. Morin-Crini, Adsorption-oriented processes using conventional and non-conventional adsorbents for wastewater treatment, in *Green Adsorbents for Pollutant Removal. Environmental Chemistry for a Sustainable World*, vol. 18, ed. by G. Crini, E. Lichtfouse (Springer, Cham, 2018)
9. M. Zimmer, Forced degradation and long-term stability testing for oral drug products: a practical approach, in *Methods for Stability Testing of Pharmaceuticals. Methods in Pharmacology and Toxicology*, ed. by S. Bajaj, S. Singh (Humana Press, New York, 2018)
10. B. Hemmateenejad, K. Javidnia, M. Saeidi-Boroujeni, J. Pharm. Biomed. Anal. **47**, 625–630 (2008)
11. M. Shamsipur, B. Hemmateenejad, M. Akhond, K. Javidnia, R. Miri, J. Pharm. Biomed. Anal. **31**, 1013–1019 (2003)
12. S. Bahrpeyma, B. Hemmateenejad, K. Javidnia, J. Iran. Chem. Soc. **13**, 221–229 (2016)
13. X. Li, J. Xie, C. Jiang, J. Yu, P. Zhang, Front. Environ. Sci. Eng. **12**, 14 (2018)
14. E. Leyva, E. Moctezuma, K.M. Baines, S. Noriega, E. Zarazua, Curr. Org. Chem. **22**, 2–17 (2018)
15. S. Stets, B. Amaral, J.T. Schneider, I.R. de Barros, M.V. de Liz, R.R. Ribeiro, N. Nagata, P. Peralta-Zamora, J. Photochem. Photobiol., A **353**, 26–33 (2018)
16. H. Ghahremani, J. Nano Res. **46**, 111–122 (2017)
17. M. Pirsaheb, A. Asadi, M. Sillanpää, N. Farhadian, J. Mol. Liq. **271**, 857–871 (2018)
18. V. Polshettiwar, R. Luque, A. Fihri, H. Zhu, M. Bouhrara, J.-M. Basset, Chem. Rev. **111**, 3036–3075 (2011)
19. D. Wang, D. Astruc, Chem. Rev. **114**, 6949–6985 (2014)
20. J.-F. Guo, B. Ma, A. Yin, K. Fan, W.-L. Dai, Appl. Catal. B **101**, 580–586 (2011)
21. J. Hu, Y. Dong, X. Chen, H. Zhang, J. Zheng, Q. Wang, X. Chen, Chem. Eng. J. **236**, 1–8 (2014)
22. C.J. Zhong, M.M. Maye, Adv. Mater. **13**, 1507–1511 (2001)
23. B. Hemmateenejad, M. Shamsipur, N. Jalili-Jahani, Photochem. Photobiol. **92**, 61–68 (2016)
24. C. Lia, R. Younesi, Y. Cai, Y. Zhu, M. Ma, J. Zhu, Appl. Catal. B **156–157**, 314–322 (2014)
25. C. Gong, Q. Li, H. Zhou, R. Liu, Colloids Surf. A **540**, 67–72 (2018)
26. X. Liu, J. Tian, Y. Li, N. Sun, S. Mia, Y. Xie, Z. Chen, J. Hazard. Mater. **373**, 397–407 (2019)
27. M.G. Alalm, S. Ookawara, D. Fukushi, A. Sato, A. Tawfik, J. Hazard. Mater. **302**, 225–231 (2016)
28. B. Özbay, N. Genç, İ. Özbay, B. Bağhaki, S. Zor, Clean Technol. Environ. Policy **18**, 2591–2601 (2016)
29. E.S. Elmolla, M. Chaudhuri, Desalination **252**, 46–52 (2010)
30. E.S. Elmolla, M. Chaudhuri, J. Hazard. Mater. **13**, 445–449 (2010)
31. Z.M. Shaykhi, A.A.L. Zinatizadeh, J. Taiwan Inst. Chem. Eng. **45**, 1717–1726 (2014)
32. E.S. Elmolla, M. Chaudhuri, J. Hazard. Mater. **12**, 1476–1481 (2009)
33. B. Priya, P. Shandilya, P. Raizada, P. Thakur, N. Singh, P. Singh, J. Mol. Catal. A **423**, 400–413 (2016)
34. B. Priya, P. Raizada, N. Singh, P. Thakur, P. Singh, J. Colloid Interface Sci. **479**, 271–283 (2016)
35. P. Raizada, J. Kumari, P. Shandilya, P. Singh, Desalin. Water Treat. **79**, 204–213 (2017)
36. G. Sharma, V.K. Gupta, S. Agarwal, S. Bhogal, M. Naushad, A. Kumar, F.J. Stadler, J. Mol. Liq. **260**, 342–350 (2018)
37. R. Nosrati, A. Olad, R. Maramifar, Environ. Sci. Pollut. Res. **19**, 2291–2299 (2012)
38. Y.L. Zhao, C.R. Tao, G. Xiao, G.P. Wei, L.H. Li, C.X. Liu, H.J. Su, Nanoscale **8**, 5313–5326 (2016)
39. B. Hemmateenejad, P. Shadabipour, T. Khosousi, M. Shamsipur, J. Ind. Eng. Chem. **27**, 384–390 (2015)
40. S.A. Hosseini, V. Majidi, A.R. Abbasian, J. Sulfur Chem. **39**, 119–129 (2018)
41. S.A. Hosseini, S. Babaei, J. Brazil. Chem. Soc. **28**, 299–307 (2017)
42. B. Hemmateenejad, P. Shadabipour, M.R. Mohamadizadeh, J. Iran. Chem. Soc. **11**, 147–154 (2014)
43. A. de Juan, J. Jaumot, R. Tauler, Anal. Methods **6**, 4964–4976 (2014)
44. Y. Zhao, Y.Q. Wei, Y. Li, B.D. Xi, Z.M. Wei, X.L. Wang, Z.N. Zhao, J. Ding, Spectrosc. Spectr. Anal. **35**, 961–965 (2015)
45. M. Sawall, A. Moog, C. Kubis, H. Schroder, D. Selent, R. Franke, A. Bracher, A. Borner, K. Neymeyr, J. Chemometr. **23**, e3012 (2018)
46. M. Garrido, F.X. Rius, M.S. Larrechi, Anal. Bioanal. Chem. **390**, 2059–2066 (2008)
47. T.R. Goncalves, L.N. Rosa, R.P. Goncalves, A.S. Torquato, P.H. Marco, S.T.M. Gomes, M. Matsushita, P. Valderrama, Food Anal. Methods **11**, 1936–1943 (2018)
48. V.T. Tran, H. Zhou, S. Lee, S.C. Hong, J. Kim, S.-Y. Jeong, J. Lee, ACS Appl. Mater. Interfaces **7**, 8650–8658 (2015)
49. H. Zhou, J. Lee, T.J. Park, S.J. Lee, J.Y. Park, J. Lee, Sens. Actuat. B **163**, 224–232 (2012)

50. K.C. Grabar, R.G. Freeman, M.B. Hommer, M.J. Natan, Anal. Chem. **67**, 735–743 (1995)
51. M. Răcuciu, D.E. Creangă, A. Airinei, Eur. Phys. J. E **21**, 117–121 (2006)
52. Q. Lan, C. Liu, F. Yang, S. Liu, J. Xu, D. Sun, J. Colloid Interface Sci. **310**, 260–269 (2007)
53. M. Spasova, V. Salgueiriño-Maceira, A. Schlachter, M. Hilgendorff, M. Giersig, L.M. Liz-Marzán, M. Farle, J. Mater. Chem. **15**, 2095–2098 (2005)
54. M. Mandal, S. Kundu, S.K. Ghosh, S. Panigrahi, T.K. Sau, S.M. Yusuf, T. Pal, J. Colloid Interface Sci. **286**, 187–194 (2005)
55. K.R. Brown, D.G. Walter, M.J. Natan, Chem. Mater. **12**, 306–313 (2000)
56. W.C. Huang, P.J. Tsai, Y.C. Chen, Small **5**, 51–56 (2009)
57. P. Singh, B. Priya, P. Shandilya, P. Raizada, N. Singh, B. Pare, S.B. Jonnalagadda, Arab. J. Chem. (2016). https://doi.org/10.1016/j.arabjc.2016.08.005
58. R. Wang, X. Wang, X. Xi, R. Hu, G. Jiang, Adv. Mater. Sci. Eng. **2012**, Article ID: 40939 (2012)
59. S. Chidambarama, B. Paria, N. Kasi, S. Muthusamy, J. Alloy Compd. **665**, 404–410 (2016)
60. M.M. Khan, J.L. Moo, H. Cho, J. Ind. Chem. Eng. **20**, 1584–1590 (2014)
61. J.P. Hou, J.W. Poole, J. Pharm. Sci. **58**, 447–454 (1969)
62. A. Olad, R. Nosrati, Res. Chem. Intermed. **41**, 1351–1363 (2015)